# An 8 month slow slip event triggers progressive nucleation of the 2014 Chile megathrust

Anne Socquet[1] iD, Jesus Piña Valdes[1] iD, Jorge Jara[1] iD, Fabrice Cotton[2,3], Andrea Walpersdorf[1] iD, Nathalie Cotte[1] iD, Sebastian Specht[2,3] iD, Francisco Ortega-Culaciati[4,5] iD, Daniel Carrizo[5], and Edmundo Norabuena[6] iD

[1]Université Grenoble Alpes, Université Savoie Mont Blanc, CNRS, IRD, IFSTTAR, ISTerre, Grenoble, France, [2]German Research Centre for Geosciences, GFZ Helmholtz Centre Potsdam, Potsdam, Germany, [3]Institute of Earth and Environmental Science, Potsdam University, Potsdam, Germany, [4]Department of Geophysics, Faculty of Physical and Mathematical Sciences, University of Chile, Santiago, Chile, [5]Advanced Mining Technology Center, Faculty of Physical and Mathematical Sciences, Universidad de Chile, Santiago, Chile, [6]Instituto Geofísico del Peru, Lima, Peru

**Abstract** The mechanisms leading to large earthquakes are poorly understood and documented. Here we characterize the long-term precursory phase of the 1 April 2014 $M_w$8.1 North Chile megathrust. We show that a group of coastal GPS stations accelerated westward 8 months before the main shock, corresponding to a $M_w$6.5 slow slip event on the subduction interface, 80% of which was aseismic. Concurrent interface foreshocks underwent a diminution of their radiation at high frequency, as shown by the temporal evolution of Fourier spectra and residuals with respect to ground motions predicted by recent subduction models. Such ground motions change suggests that in response to the slow sliding of the subduction interface, seismic ruptures are progressively becoming smoother and/or slower. The gradual propagation of seismic ruptures beyond seismic asperities into surrounding metastable areas could explain these observations and might be the precursory mechanism eventually leading to the main shock.

## 1. Introduction

Some earthquakes have been preceded by an intense foreshock activity [*Bouchon et al.*, 2013; *Schurr et al.*, 2014; *Ruiz et al.*, 2014; *Lay et al.*, 2014; *Bedford et al.*, 2015; *Cesca et al.*, 2016; *Kato et al.*, 2016; *Meng et al.*, 2015; *Hasegawa and Yoshida*, 2015; *Kato et al.*, 2012; *Ozawa et al.*, 2012, *Sato et al.*, 2013; *Bouchon et al.*, 2011] raising the possibility that earthquake forecasting may be achieved through a better understanding of precursory mechanisms. Two concurrent models have been proposed to explain the initiation of seismic rupture [*Dodge et al.*, 1996]. A first model assumes that the accelerated moment release observed before large earthquakes [*Bowman and King*, 2001] is triggered by a slow slip event on the fault interface [*Bouchon et al.*, 2013; *Ruiz et al.*, 2014; *Dodge et al.*, 1996]. Alternatively a slow cascade of failures eventually may trigger the main shock [*Dodge et al.*, 1996].

The precursory phase of earthquakes is most usually studied using seismological data, which is readily available in some regions. Because of limited in situ monitoring combined with lower detection thresholds, geodetic data are less commonly used to study earthquake precursors. Therefore, the link between foreshock activity and associated deformation transients has never been directly established for periods exceeding a few weeks, although it has been observed and suggested [*Obara and Kato*, 2016, and references therein].

The $M_w$8.1 2014 Iquique earthquake occurred within the North Chile seismic gap, which had not experienced a megathrust rupture since 1877 [*Bejar Pizarro et al.*, 2013; *Metois et al.*, 2016]. The earthquake ruptured an ~ 150 km long portion of the subduction zone [*Schurr et al.*, 2014; *Ruiz et al.*, 2014], in an area that was partially locked before the earthquake [*Bejar Pizarro et al.*, 2013; *Metois et al.*, 2016]. The earthquake was preceded by a series of earthquake swarms beginning in July 2013 [*Schurr et al.*, 2014; *Ruiz et al.*, 2014].

Given the presence of detailed seismic and geodetic monitoring of the Chilean subduction zone, this earthquake is an excellent case to monitor the precursory seismic activity and associated deformation. Previous studies focused mostly on the 20 days immediately preceding the earthquake when a strong transient signal occurred [*Schurr et al.*, 2014; *Ruiz et al.*, 2014; *Lay et al.*, 2014; *Bedford et al.*, 2015; *Cesca et al.*, 2016]. Nevertheless, a debate remains on the mechanisms leading to this foreshock activity, notably on the existence or not of aseismic slip preceding the earthquake. Apart from the study of the foreshock
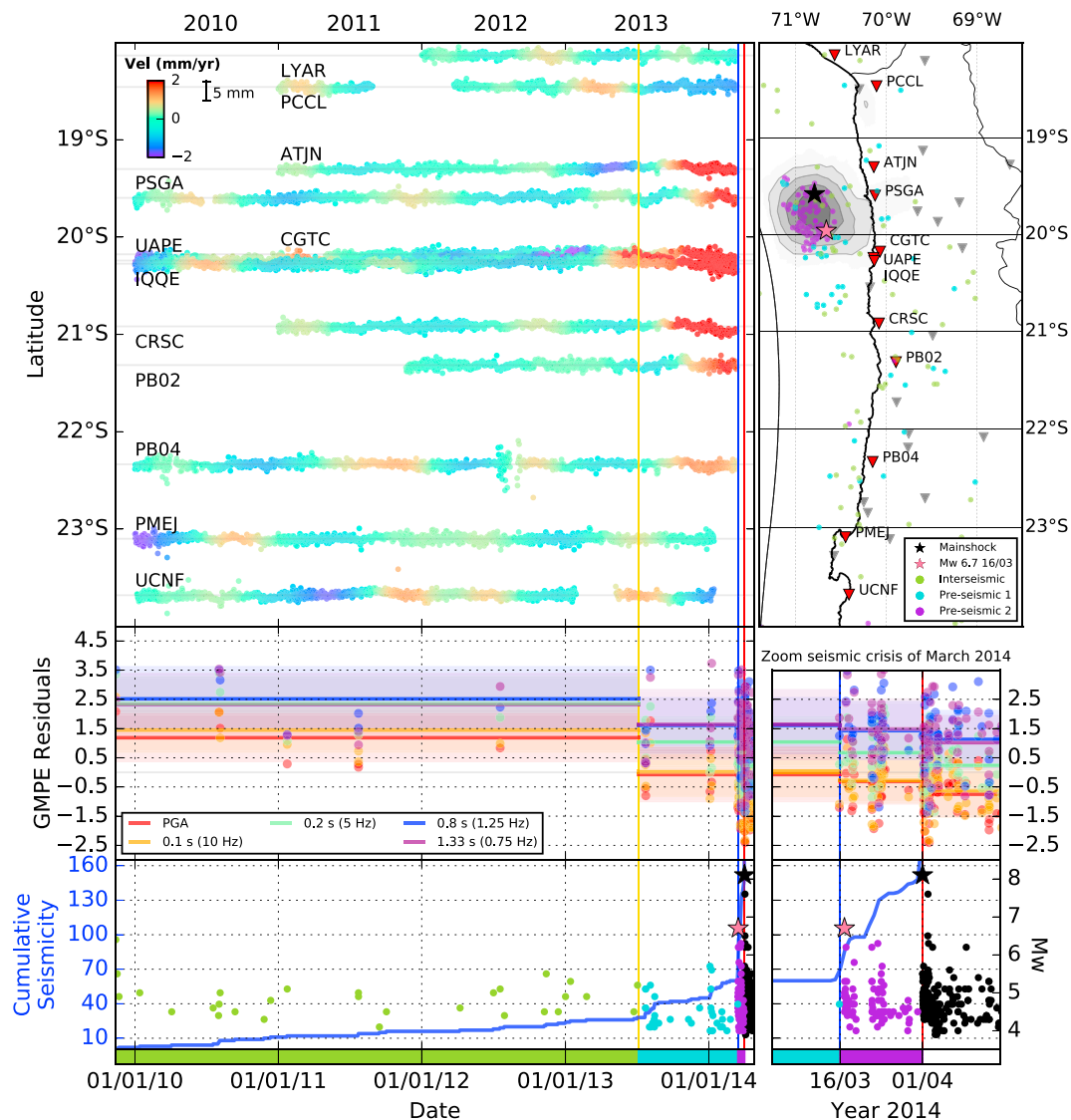
**Figure 1.** Preseismic ground deformation and foreshock frequency content over a 4 year period, before the 1 April 2014 megathrust in North Chile. (top right) Map of seismicity: foreshock activity color coded by periods, epicenters of $M_w$8.1 main shock and $M_w$6.7 foreshock are indicated by black and pink stars, $M_w$8.1 slip distribution with 1 m contours. Triangles indicate the location of GPS stations, the red ones being stations whose time series are shown to the left. (top left) Trench perpendicular, detrended time series of coastal cGPS, sorted by latitude. Colors show the variation of average GPS velocities computed in 6 month sliding windows. (middle left) Frequency content evolution of interface foreshocks. Lines show average values of normalized residuals with respect to GMPE model [*Abrahamson et al.*, 2015] at high (reddish) and low (bluish) frequencies computed for each time period. Standard deviation of the model is shown by shaded colors, while dots show single earthquakes residuals. (bottom left) Foreshock activity over time (dots). Blue curve shows the cumulative number of earthquakes. Red, blue, and yellow vertical lines separate the three preseismic periods and depict respectively the $M_w$8.1 main shock on 1 April 2014, the $M_w$6.7 foreshock of 16 March 2014 that is followed by an increase of seismicity rate 2 weeks before the main shock, and the July 2013 swarm.

sequence [*Schurr et al.*, 2014; *Ruiz et al.*, 2014; *Lay et al.*, 2014; *Bedford et al.*, 2015; *Cesca et al.*, 2016; *Kato et al.*, 2016; *Meng et al.*, 2015], very little is known about any potential long-term precursors, in particular in terms of deformation.

Here we use geodetic and seismological observations to document the precursory deformation and foreshock frequency content for the 2 years preceding the Iquique earthquake.

## 2. Data and Methods

GPS data from several networks monitoring the North Chile subduction (IPOC, LIA Montessus de Ballore, ISTerre, Caltech Andean Observatory, IGS) have been processed in double differences, including
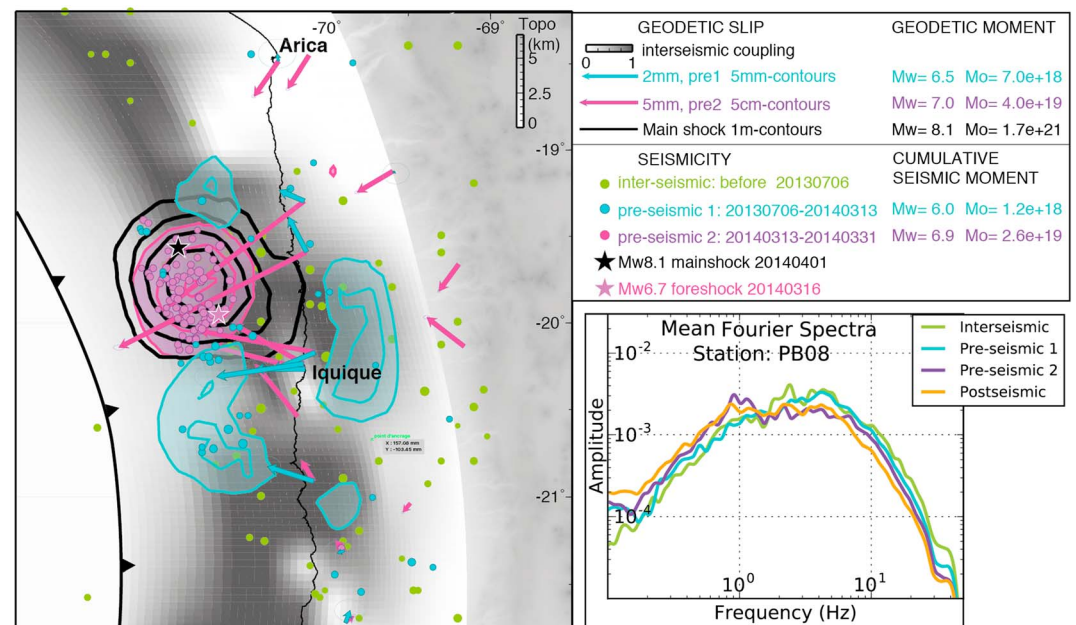
**Figure 2.** (left) Long- and short-term slip events (in blue and purple, respectively), preceding the $M_w8.1$ main shock, superimposed on the interseismic coupling distribution [*Metois et al.,* 2016] in gray, and the coseismic slip 1 m contours in black. Foreshock seismic activity for the same periods is also shown (in blue, purple, and green, $M_w > 4$). Epicenters of the main shock and the $M_w6.7$ foreshock are shown as black and pink stars. (right inset) Mean Fourier spectra computed for interface earthquakes ($5.1 < M_w < 5.2$) grouped into four different time periods: interseismic in green, preseismic 1 in cyan, preseismic 2 in purple, and postseismic in orange. Station PB08 being located at an even distance of the earthquakes studied, the computed variations in Fourier spectra shapes should be unaffected by variations in attenuation but, instead, characterize earthquake's source.

tropospheric delays and gradients [*Boehm et al.,* 2006], and mapped into the ITRF 2008 [*Altamimi et al.,* 2011] (see supporting information for further details). The trend, as well as seasonal signals and common modes were removed from the time series. In order to study the long-term transient in our time series, we excluded data after 15 March 2014 (when a strong preseismic signal occurred) and then computed the average velocity variations, by fitting a linear regression in a 6 month sliding window of the detrended and denoised time series (Figure 1). In a second step, we compute the displacement during two preseismic periods (preseismic 1: July 2013 to 13 March 2014 and preseismic 2: 14 March 2014 to 31 March 2014), by taking as a reference the mean interseismic loading trend before July 2013 (Figures S2 and S3).

The surface deformation fields were then inverted to retrieve the distribution of slip on the subduction interface (Figure 2), by discretizing it as a series of dislocations buried in a layered elastic half space [*Wang et al.,* 2003]. A Laplacian smoothing has been applied; the best compromise between model roughness and data-model misfit has been chosen [*Jonsson et al.,* 2002]. The power of our data to constrain the slip on the interface [*Loveless and Meade,* 2011] is high from 15 km depth to more than 70 km depth in general (Figures S4–S6). Although the details of slip distributions can vary from one inversion to the other, the estimated geodetic moment of preseismic slow slip events vary within less than 10% (Figure S7).

To complement the geodetic analysis, we analyzed the frequency content of interface seismicity. The interface seismicity catalog (Figure S9) was compiled using the GEOFON moment tensor catalog and the Global CMT catalog. We use a data driven algorithm to automatically determine focal mechanism clusters with similar style of faulting (strike, rake, and dip, Figure S10).

The horizontal response and Fourier spectra of interface earthquakes were computed from the acceleration records of stations belonging to the IPOC network (Figure S9). The raw acceleration records were demeaned and tapered, and a zero pad has been applied at the beginning and the end before being

used to compute the spectra [*Boore et al.*, 2012; *Chiou et al.*, 2008]. The response spectra were also computed for each horizontal component of the records following the *Nigam and Jennings* [1969] method with a damping of 5%. Finally, both Fourier and response horizontal spectra were computed as the geometrical mean of the two horizontal response spectra at each station. Fourier source spectra depend on source, propagations, and site effects. Also, there is then a need to deconvolve the records from propagation and site properties to analyze earthquake source properties. In order to compare the shape of Fourier spectra during the different time span studied, we selected three IPOC stations located at equal distance from the earthquakes swarm to get rid of the attenuation effects and performed our analysis on earthquakes within a 0.1 magnitude range (Figures S11 and 2 (right inset)).

Second, we compared the measured ground accelerations, at different frequencies, with the response spectra predicted by the recent Ground Motion Prediction Equation (GMPE) developed for subduction interface earthquakes by *Abrahamson et al.* [2015]. *Abrahamson et al.*'s [2015] model is recognized as one of the leading models to predict ground motions in subduction areas and has been recently selected for the Global Earthquake Model [*Stewart et al.*, 2015]. The analysis of the obtained residuals confirmed that this model is well suited for our data set (see supporting information for details). Between-event residuals were computed, for each frequency (0.75 Hz, 1 Hz, 1.25 Hz, 5 Hz, 10 Hz, and PGA) and each earthquake, as the difference between the median of the observations of the given earthquake and the median of the model [*Abrahamson and Youngs*, 1992]. The Ground Motion Prediction Equations is acting here as a backbone model which takes into account first-order magnitude and propagation effects. The analysis of relative time and spatial variations of between-event residuals allow us to compare the source effects of earthquakes with various magnitude and locations [*Strasser et al.*, 2010, *Atik et al.*, 2010; *Youngs et al.*, 1995]. It has been shown that response between-event residuals are fully correlated with "classical" Fourier stress drops [*Bindi et al.*, 2007], so there is no information lost using response spectra and GMPEs compared to a more classical stress drop analysis. The between-event residuals were then organized as a function of time, space, and magnitude, in order to represent their variations and temporal evolution during the different periods before or after the main shock (Figures 3 and S15).

## 3. Results

### 3.1. Precursory Slow Slip and Associated Seismicity

We detected a westward acceleration of some permanent GPS stations with respect to the average interseismic velocity (Figure 1). This acceleration begins ~8 months before the main shock and affects mostly coastal stations located within an area 100 km south of the $M_w 8.1$ source, which was also affected by foreshock seismicity during the same period (Figure 1, blue dots). For comparison, during the preceding interseismic period, the seismicity is evenly distributed within the deeper part of the seismogenic zone (green dots in Figures 1 and 2). Inversion of these 8 month preseismic displacements (from July 2013 to mid-March 2014) suggests that a slow slip event occurred on the subduction interface (Figure 2, blue contours), surrounding the main shock slip patch. South of the main shock, the slow slip occurs in a zone of low coupling during the interseismic period [*Metois et al.*, 2016], while it rather affects areas characterized by intermediate locking downdip and north of the main shock. The geodetic precursor is collocated with long-term foreshock activity (Figure 2, blue dots). The comparison between geodesy and seismology shows that this long-term preseismic signal is at least 80% aseismic in nature; the cumulative seismic moment release ($1.2 \times 10^{18}$ N m) representing 17 to 19% of the slip derived from GPS observations ($6.4$ to $7.0 \times 10^{18}$ N m).

On 16 March 2014, a $M_w 6.7$ intraplate earthquake [*Cesca et al.*, 2016] occurred 2 weeks before the main shock, north of the creeping area (pink star, Figure 2). This foreshock is the largest of the whole sequence. It is followed by an abrupt increase of the seismicity rate and associated $b$ value [*Schurr et al.*, 2014], some of them in the upper plate, and most of them on the subduction interface [*Cesca et al.*, 2016], affecting the area that later ruptured during the $M_w 8.1$ megathrust. During this 15 day preseismic period, GPS stations were affected by a large deformation transient [*Ruiz et al.*, 2014] (Figure 2). This preseismic slip measured by geodesy resembles the one released seismically: the location and shape of geodetic slip mimics the spatial distribution of epicenters (Figure 2, purple contours and dots) [*Schurr et al.*, 2014], while the seismic moment is 65–67% of the geodetic moment (the remaining 33–35% is aseismic).
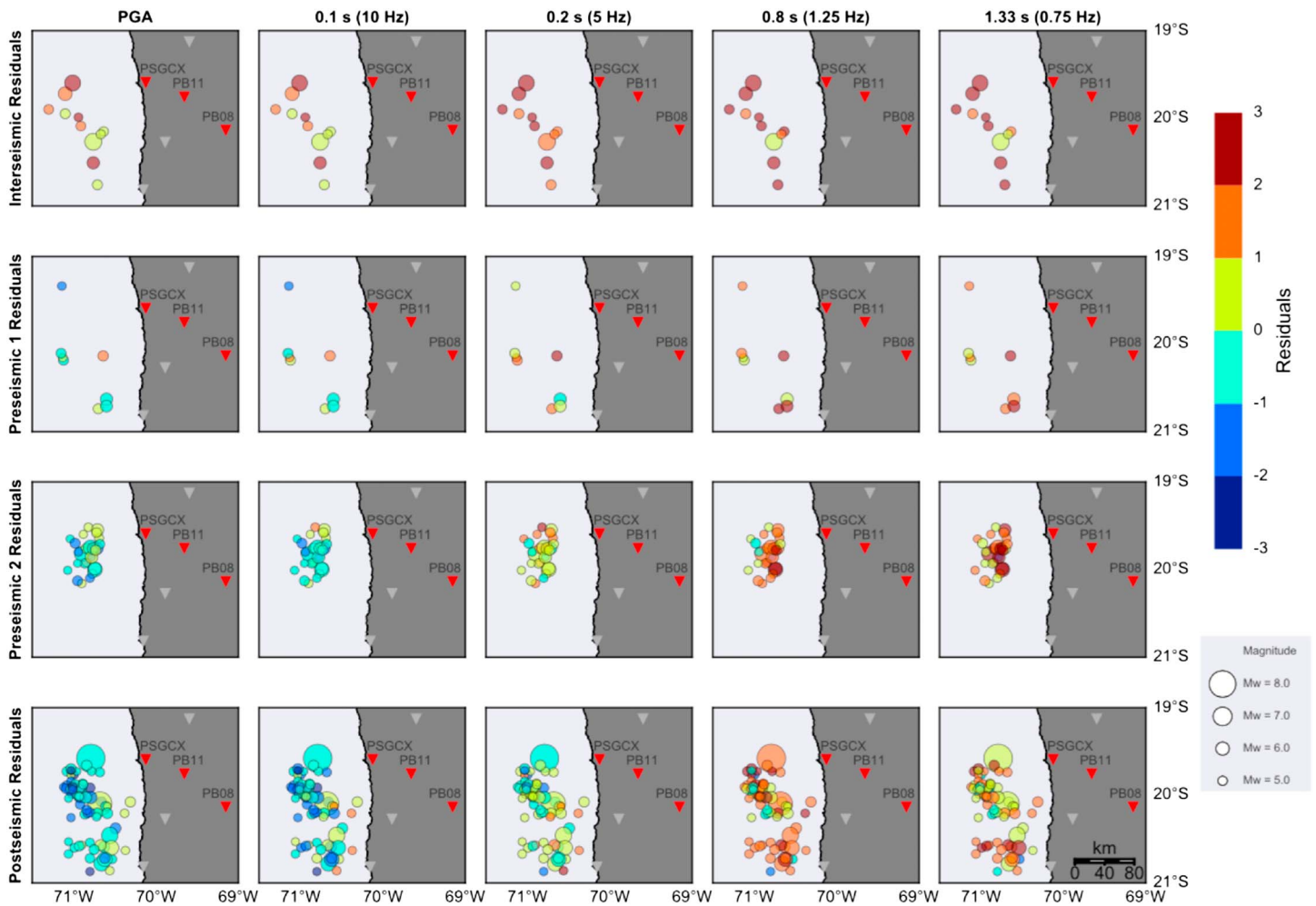
**Figure 3.** Time-space evolution of between-event residuals at the different frequency values shown in Figure 1 (middle row). Residuals are normalized by the standard deviation of the GMPE model. Therefore, average temporal changes can be considered significant from one standard deviation.

### 3.2. Evolution of Interface Earthquakes Ground Motions

To complement these findings, we analyzed the frequency content of interface seismicity [*Specht et al.,* 2017; *Strasser et al.,* 2009]. Mean Fourier spectra at stations equidistant to the seismic crisis events show a consistent temporal decrease in high frequencies from interseismic to preseismic and, eventually, postseismic periods (Figures 2 and S11).

The comparison of the measured accelerations for interface earthquakes with respect to the ground motion model [*Abrahamson et al.,* 2015] provides an independent assessment of ground motion temporal variations [*Händel et al.,* 2014]. The time, space, and magnitude dependencies of between-event residuals have been analyzed in order to search for a potential evolution of the source characteristic (Figures 3 and S15). Measured residuals do not depend on earthquakes magnitude (as expected given the fact that the ground motion predictive equation acts as a backbone model correcting for magnitude and propagation effects). However, at frequencies of 5 Hz and above, a clear clustering of between-event residuals as a function of their time of occurrence is observed (Figure S15), indicating a diminution of high-frequency energy release from interseismic period to preseismic period and later. Also, the temporal evolution of residuals differs from one frequency band to the other: at frequencies below 1.25 Hz residuals remain more or less constant with time, while at higher frequencies (5 Hz and above) residuals decrease between interseismic period to preseismic and postseismic periods (Figures 1–3). During the second preseismic period (i.e., during the 15 days between the largest foreshock and the main shock) and the postseismic period, interface earthquakes show no significant change of their energy radiation.
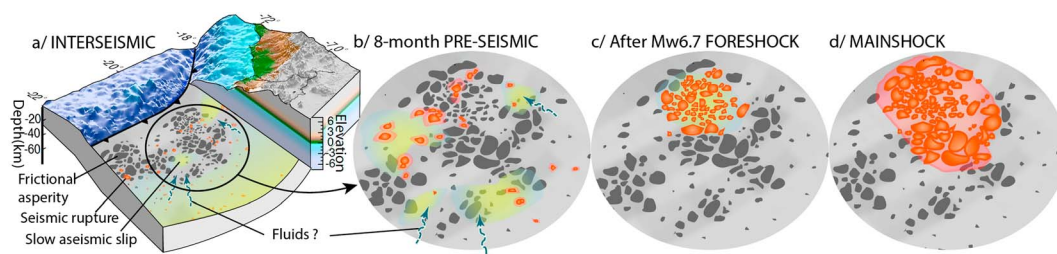
**Figure 4.** Schematic interpretation of the precursory phase of $M_w$8.1 earthquake. (a) During the interseismic phase, the subduction interface slowly creeps (yellow) at depth and in low coupling areas, where frictional asperities are sparse. The rupture of small frictional asperities resisting this slow slip generates the background seismicity (red). (b) Eight months before the main shock, slow slip accelerates in the seismogenic zone (maybe facilitated by fluids migration), around the area ruptured by the main shock. Seismic ruptures start to propagate into the conditionally stable area surrounding the frictional asperities (light red). (c) After the largest foreshock on 16 March ($M_w$6.7), slow slip goes on but is superimposed onto a rough seismic signal generated by the postseismic cascade. (d) On 1 April 2014, $M_w$8.1 earthquake ruptures a large portion of the subduction interface, breaking both frictional asperities (red) and surrounding conditionally stable areas (light red).

These two independent assessments of interface earthquake ground motions indicate a reduction of the high-frequency radiation, which is coincident with the preseismic acceleration in GPS velocities 8 months before the main shock.

## 4. Discussion

Our results indicate that a geodetic precursor occurred simultaneously with an identified increase in the seismicity rate (Figure 1, bottom row), and a decrease in the *b* value [*Schurr et al.*, 2014]. Such observations can be modeled as an aseismic slow slip on the subduction interface collocated with long-term foreshock activity (Figure 2, blue dots). This is consistent with the slow sliding of conditionally stable area on the subduction interface, spread out by sparse, small seismic asperities [*Hetland and Simons*, 2010], the seismic activity arising from the response of seismic asperities to the aseismic forcing.

Seismic radiation spectra of interface events have been proposed, on average, to be representative of the different frictional regimes of a subduction interface [*Scholz*, 1998; *Lay et al.*, 2012]; regions of unstable sliding can have large slip but generate modest amounts of short-period radiation upon failure, while smaller patchy regions of unstable sliding produce coherent short-period radiation when loaded to failure by creep of conditionally stable surrounding regions [*Lay et al.*, 2012; *Meng et al.*, 2015].

The reduction in high-frequency radiated energy often indicates a reduction in earthquake stress drop (i.e., a decrease of corner frequency). This phenomenon might be explained either by (a) smoother ruptures [*Radiguet et al.*, 2009], (b) lower rupture velocities, or (c) increasing high-frequency attenuation. Given the foreshocks sequence does not migrate through time, a change in attenuation characteristics over such a short period of time seems unlikely. Rapid fluid migration within the fault zone may change the attenuation locally, within the few hundred meters of the damaged fault zone (high pore fluid pressures are accompanied by very low Qs/Qp ratios—0.1 to 0.4 for saturated basalt that are primarily due to increased shear attenuation [*Tompkins and Christensen*, 2001]). However, once integrated over the whole path followed by seismic waves through continental crust (a few hundred meters with increased attenuation versus tens of kilometers with no change), this local change in attenuation accounts for a minor part of the overall attenuation and only at large frequencies (higher than 15–20 Hz). It will be considered as part of the source, distance independent, high-frequency (kappa) attenuation. Therefore, the observed change of frequency content at 5–10 Hz rather seems related to a modification of the earthquake source parameters, such as a wider rupture area or slower rupture velocity. This is also compatible with the observed reduction in *b* value during the precursory time period, implying an increasing proportion of large to small earthquakes. Such a decrease in *b* value has been proposed as a precursor to major macrofailure [*Smith*, 1981]. Our observations suggest that a slow aseismic forcing that started 8 months before the main shock triggered an increased number of seismic events together with a modification of the earthquake frequency content, interpreted as a widening of rupture surfaces [*Lay et al.*, 2012]. This suggests a progressive expansion of failures into the conditionally stable areas surrounding small seismic asperities, in a mechanism that will eventually lead to the main rupture nucleation (Figure 4b).

Two weeks before the main shock, the largest foreshock of the sequence triggered an increased deformation, seismicity, and $b$ value. This seismicity, which is much more focused both spatially and temporally, might have been triggered by the $M_w$6.7 foreshock that induced a significant increase of the Coulomb stress in the area. The seismicity and associated slow slip observed within the 15 days before the main shock may therefore result from a regular aftershock sequence and associated afterslip following the $M_w$6.7 event, overprinting the preexisting slow aseismic slip (Figure 4c).

On 1 April 2014, the $M_w$8.1 megathrust nucleates immediately north of the seismicity surge, in an area of increased stress resulting from adjacent preseismic slip. The maximum slip (Figure 2, black contours) occurs close to the area that started to slip before the main shock (pink), slightly downdip associated foreshock activity (pink dots), including repeating earthquakes [*Meng et al.*, 2015]. However, the rupture extends deeper to areas that were fully locked during the interseismic period [*Metois et al.*, 2016]. To the south, the rupture stops abruptly when it reaches the metastable areas affected by the long-term aseismic precursor (blue).

## 5. Conclusions

These observations confirm that a long-term aseismic slip of the subduction interface led to the nucleation of the $M_w$8.1 Iquique megathrust earthquake. During the interseismic period, the seismicity was evenly distributed within the deeper part of the seismogenic zone (green dots on Figures 1 and 2) and ruptured small frictional asperities in response to deep interplate aseismic sliding (Figure 4). Eight months before the main shock, this slow sliding of plate interface started to accelerate within the seismogenic zone. South of the main shock this precursory creep occurs in an area characterized by little interseismic coupling, while downdip and north of the main shock, the slow slip affects more coupled areas (Figure 2) [*Metois et al.*,2016] and may be seen as the slow rupture of locked patches surrounding the main shock. Small seismic asperities scattered in this area ruptured repeatedly [*Meng et al.*, 2015; *Lay et al.*, 2012]. The change in the earthquake frequency content during the foreshock sequence (a reduction of the stress drop) suggests that seismic failures widen progressively, decelerate, and start to extend into the slowly sliding, conditionally stable areas surrounding frictional asperities. This process can be seen as the start of the precursory phase that will eventually lead to the megathrust rupture.

The simultaneous occurrence of slip acceleration, increased seismic activity, and the slow decrease of the high-frequency radiations of foreshocks may provide a way to detect the preparation of great earthquakes. Identifying aseismic slip combined with changes in associated earthquake spectra may therefore significantly help to mitigate seismic hazard at plate boundaries.

## References

Abrahamson, N., N. Gregor, and K. Addo (2015), BC Hydro ground motion prediction equations for subduction earthquakes, *Earthquake Spectra*, doi:10.1193/051712EQS188MR.

Abrahamson, N. A., and R. R. Youngs (1992), A stable algorithm for regression analyses using the random effects model, *Bull. Seismol. Soc. Am.*, *82*, 505–510.

Altamimi, Z., X. Collilieux, and L. Métivier (2011), ITRF2008: An improved solution of the international terrestrial reference frame, *J. Geod. 85*, 457–473, doi:10.1007/s00190-011-0444-4.

Atik, L. A., N. Abrahamson, J. J. Bommer, F. Scherbaum, F. Cotton, and N. Kuehn (2010), The variability of ground-motion prediction models and its components, *Seismol. Res. Lett.*, *81*(5), 794–801, doi:10.1785/gssrl.81.5.794

Bedford, J., M. Moreno, B. Schurr, M. Bartsch, and O. Oncken (2015), Investigating the final seismic swarm before the Iquique-Pisagua 2014 $M_w$8.1 by comparison of continuous GPS and seismic foreshock data, *Geophys. Res. Lett.*, *42*, 3820–3828, doi:10.1002/2015GL063953.

Bejar Pizarro, M., A. Socquet, R. Armijo, D. Carrizo, J. Genrich, and M. Simons (2013), Andean structural control on interseismic coupling in the North Chile subduction zone, *Nat. Geosci.*, doi:10.1038/NGEO1802.

Bindi, D., S. Parolai, E. Görgün, H. Grosser, C. Milkereit, M. Bohnhoff, and E. Durukal (2007), ML scale in northwestern Turkey from 1999 Izmit aftershocks: Updates, *Bull. Seismol. Soc. Am.*, *97*(1B), 331–338, doi:10.1785/0120060071.

Boehm, J., B. Werl, and H. Schuh (2006), Troposphere mapping functions for GPS and very long baseline interferometry from European Centre for Medium-Range Weather Forecasts operational analysis data, *J. Geophys. Res. 111*, B02406, doi:10.1029/2005JB003629.

Boore, D. M., A. A. Sisi, and S. Akkar (2012), Using pad stripped acausally filtered strong motion data, *Bull. Seismol. Soc. Am.*, *102*(2), 751–760.

Bouchon, M., H. Karabulut, M. Aktar, S. Özalaybey, J. Schmittbuhl, and M. P. Bouin (2011), Extended nucleation of the 1999 $M_w$ 7.6 Izmit earthquake, *Science*, *331*(6019), 877–880, doi:10.1126/science.1197341.

Bouchon, M., V. Durand, D. Marsan, H. Karabulut, and J. Schmittbuhl (2013), The long precursory phase of most large interplate earthquakes, *Nat. Geosci.*, *6*(4), 299–302, doi:10.1038/NGEO1770.

Bowman, D. D., and G. C. P. King (2001), Accelerating seismicity and stress accumulation before large earthquakes, *Geophys. Res. Lett.*, *28*, 4039–4042, doi:10.1029/2001GL013022.

Cesca, S., F. Grigoli, S. Heimann, T. Dahm, M. Kriegerowski, M. Sobiesiak, C. Tassara, and M. Olcay (2016), The $M_w$ 8.1 2014 Iquique, Chile, seismic sequence: A tale of foreshocks and aftershocks, *Geophys. J. Int.*, *204*(3), 1766–1780.

Chiou, B., R. Darragh, N. Gregor, and W. Silva (2008), NGA project strong-motion database, *Earthquake Spectra*, *24*(1), 23–44.

Dodge, D. A., G. C. Beroza, and W. L. Ellsworth (1996), Detailed observations of California foreshock sequences: Implications for the earthquake initiation process, *J. Geophys. Res.*, *101*, 22,371–22,392, doi:10.1029/96JB02269.

Händel, A., S. Specht, N. M. Kühn, and F. Scherbaum (2014), Mixtures of ground-motion prediction equations as backbone models for a logic tree: An application to the subduction zone in Northern Chile, *Bull. Earthq. Eng.*, *13*(2), 483–501, doi:10.1007/s10518-014-9636-7.

Hasegawa, A., and K. Yoshida (2015), Preceding seismic activity and slow slip events in the source area of the 2011 $M_w$ 9.0 Tohoku-Oki earthquake: A review, *Geosci. Lett.*, *2*(1), 6, doi:10.1186/s40562-015-0025-0.

Hetland, E. A., and M. Simons (2010), Post-seismic and interseismic fault creep: II. Transient creep and interseismic stress shadows on megathrusts, *Geophys. J. Int.*, *181*, 99–112, doi:10.1111/j.1365-246X.2009.04482.x.

Jonsson, S., H. Zebker, P. Segall, and F. Amelung (2002), Fault slip distribution of the 1999 $M_w$ 7.1 hector mine, California, earthquake, estimated from satellite radar and GPS measurements, *Bull. Seismol. Soc. Am.*, *92*(4), 1377–1389, doi:10.1785/0120000922.

Kato, A., K. Obara, T. Igarashi, H. Tsuruoka, S. Nakagawa, and N. Hirata (2012), Propagation of slow slip leading up to the 2011 $M_w$ 9.0 Tohoku-Oki earthquake, *Science*, *335*(2), 705–708, doi:10.1126/science.1215141.

Kato A. et al. (2016), Accelerated nucleation of the 2014 Iquique, Chile $M_w$ 8.2 earthquake, *Nat. Sci. Rep.*, *6*, 24792, doi:10.1038/srep24792.

Lay, T., H. Kanamori, C. J. Ammon, K. D. Koper, A. R. Hutko, L. Ye, H. Yue, and T. M. Rushing (2012), Depth-varying rupture properties of subduction zone megathrust faults, *J. Geophys. Res.*, *117*, B04311, doi:10.1029/2011JB009133.

Lay, T., H. Yue, E. E. Brodsky, and C. An (2014), The 1 April 2014 Iquique, Chile, $M_w$ 8.1 earthquake rupture sequence, *Geophys. Res. Lett.*, *41*, 3818–3825, doi:10.1002/2014GL060238.

Loveless, J. P., and B. J. Meade (2011), Spatial correlation of interseismic coupling and coseismic rupture extent of the 2011 $M_W$ = .0 Tohoku Oki earthquake, *Geophys. Res. Lett.*, *38*, L17306, doi:10.1029/2011GL048561.

Meng, L., H. Huang, R. Bürgmann, J. P. Ampuero, and A. Strader (2015), Dual megathrust slip behaviors of the 2014 Iquique earthquake sequence, *Earth Planet. Sci. Lett.*, *411*, 177–187, doi:10.1016/j.epsl.2014.11.041

Metois, M., C. Vigny, and A. Socquet (2016), Interseismic coupling, megathrust earthquakes and seismic swarms along the Chilean subduction zone (38°–18°S), *Pure Appl. Geophys.*, *194*(3), 1283–1294, doi:10.1007/s00024-016-1280-5.

Nigam, N. C., and P. C. Jennings (1969), Calculation of response spectra from strong-motion earthquake records, *Bull. Seismol. Soc. Am.*, *59*(2), 909–922.

Obara, K., and A. Kato (2016), Connecting slow earthquakes to huge earthquakes, *Science*, *353*(6296), 253–257, doi:10.1126/science.aaf1512.

Ozawa, S., T. Nishimura, H. Munekane, H. Suito, T. Kobayashi, M. Tobita, and T. Imakiire (2012), Preceding, coseismic, and postseismic slips of the 2011 Tohoku earthquake Japan, *J. Geophys. Res.*, *117*, B07404, doi:10.1029/2011JB009120.

Radiguet, M., F. Cotton, I. Manighetti, M. Campillo, and J. Douglas (2009), Dependency of near-field ground motions on the structural maturity of the ruptured faults, *Bull. Seismol. Soc. Am.*, *99*(4), 2572–2581.

Ruiz, S., M. Metois, A. Fuenzalida, J. Ruiz, F. Leyton, R. Grandin, C. Vigny, R. Madariaga, and J. Campos (2014), Intense foreshocks and a slow slip event preceded the 2014 Iquique $M_w$ 8.1 earthquake, *Science*, doi:10.1126/science.1256074.

Sato, T., S. Hiratsuka, and J. Mori (2013), Precursory seismic activity surrounding the high-slip patches of the 2011 $M_w$ 9.0 Tohoku-Oki earthquake, *Bull. Seismol. Soc. Am.*, *106*(6), 3104–3114, doi:10.1785/0120130042.

Scholz, C. H., Earthquakes and friction laws, *Nature*, *391*, 37–42 (1998) doi:10.1038/34097.

Schurr, B., et al. (2014), Gradual unlocking of plate boundary controlled initiation of the 2014 Iquique earthquake, *Nature*, doi:10.1038/nature13681.

Smith, W. D., The *b*-value as an earthquake precursor, *Nature*, *289*, 136–139 (1981) doi:10.1038/289136a0.

Specht, S., O. Heidbach, F. Cotton, and A. Zang (2017), Data-driven earthquake focal mechanism cluster analysis, *Sci. Tech. Rep. STR; 17/01*, Potsdam : GFZ German Res. Cent. for Geosci., doi:10.2312/GFZ.b103-17012.

Stewart, J. P., J. Douglas, M. Javanbarg, Y. Bozorgnia, N. A. Abrahamson, D. M. Boore, K. W. Campbell, E. Delavaud, M. Erdik, and P. J. Stafford (2015), Selection of ground motion prediction equations for the global earthquake model, *Earthquake Spectra*, *31*, 1, 19–45, doi:10.1193/013013EQS017M.

Strasser, F. O., N. A. Abrahamson, and J. J. Bommer (2009), Sigma: Issues, insights, and challenges, *Seismol. Res. Lett.*, *80*(1), 40–56. doi:10.1785/gssrl.80.1.40

Strasser, F. O., M. C. Arango, and J. J. Bommer (2010), Scaling of the source dimensions of interface and intraslab subduction-zone earthquakes with moment magnitude, *Seismol. Res. Lett.*, *81*, 941–950.

Tompkins, M. J., and N. I. Christensen (2001), Ultrasonic *P*- and *S*-wave attenuation in oceanic basalt, *Geophys. J. Int.*, *145*(1), 172–186, doi:10.1046/j.0956-540x.2001.01354.x.

Wang, R., F. Lorenzo-Martín, and F. Roth (2003), Computation of deformation induced by earthquakes in a multi-layered elastic crust—FORTRAN programs EDGRN/EDCMP, *Comput. Geosci.*, *29*(2), 195–207.

Youngs, R. R., N. Abrahamson, F. I. Makdisi, and K. Sadigh (1995), Magnitude-dependent variance of peak ground acceleration, *Bull. Seismol. Soc. Am.*, *85*(4), 1161–1176.